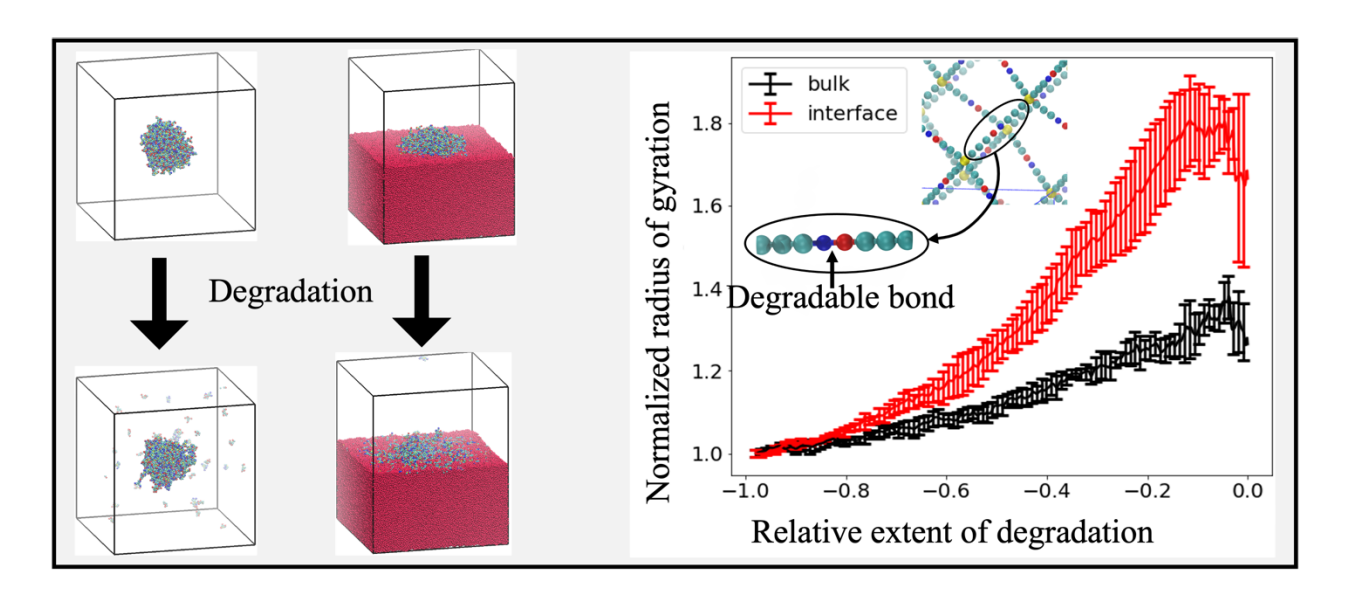
Nanogel degradation at soft interfaces and in bulk: tracking shape changes and interfacial spreading

Vaibhav Palkar¹, Devanshu Thakar^{1,2}, Olga Kuksenok^{1,*}

¹Department of Materials Science and Engineering, Clemson University, Clemson, South Carolina 29634, United States

² Department of Chemical Engineering, Indian Institute of Technology, Gandhinagar, 382055, India

: okuksen@clemson.edu



For Table of Contents use only

Abstract

Via mesoscale simulations, we characterize the process of controlled degradation of nanogels suspended in a single solvent and those adsorbed at the liquid-liquid interface between two incompatible fluids. Controlled degradation is of interest since it can be used to dynamically tailor size, shape, and transport properties of these soft particles. For the nanogels adsorbed at the liquid-liquid interfaces, controlled degradation can provide a means to dynamically tailor interfacial properties at the nanoscale. To characterize degradation process, we track the structural characteristics of the remnant nanogel, such as its radius of gyration and shape anisotropy, and spaciotemporal distribution of the broken-off fragments. We use Dissipative Particle Dynamics (DPD) approach with an adapted form of the modified Segmental Repulsive Potential (mSRP). We identify reverse gel point and characterize the scaling of this point with the finite number of polymer precursors in the system. Further, we characterize the effects of polymer-solvent interactions on the evolution of shape and effective size of the nanogel during the degradation process. We show that for the nanogel adsorbed onto the liquid-liquid interface the extent of spreading is controlled by the relative extent of degradation. We demonstrate that depending on the properties of the soft interface, broken-off fragments can either disperse into one of the phases or adsorb onto the interface enhancing the interfacial coverage and controlling interfacial properties at the nanoscale. Our study provides insights into using controlled degradation to dynamically tune shapes of nanocarriers and nanoscale topography at the liquid-liquid interfaces.

Introduction

Nanogels and microgels find their uses in a broad range of applications including drugs and biomolecules delivery and controlled release^{1, 2}, catalyst carriers³, interfacial catalysis⁴, stimuli responsive emulsion stabilizers⁵, and fabrication of scaffolds for cells and tissue culture⁶. These polymeric particles can be fabricated of various shapes, sizes, softness^{5, 7}, and with tailored stimuli-responsive functionalities. Recent advances in synthesis of functional nanogels and microgels and their applications are surveyed in a number of recent reviews⁷⁻⁹. The equilibrium size of a microgel swollen in a solvent depends on solvent quality and is defined by the balance between the osmotic and elastic contributions to the stress tensor. This balance can be externally controlled for a broad range of stimuli-responsive hydrogel networks that can respond to environmental changes such as changes in pH¹⁰, temperature^{10, 11}, and external light¹². As an example, thermoresponsive poly(N-isopropylacrylamide)-based gels undergo a temperature induced volume phase transition resulting in a fraction of water being expelled from the network, ultimately causing a particle collapse and respective reduction in microgel size10, 11, 13. Photodegradation of nanogels and microgels can be used to remotely control drug delivery¹⁴ or to control properties of scaffolds for multidimensional cell culture⁶.

Nanogels and microgels are also extensively used in multi-component systems with two incompatible liquids, where the particles adsorb onto and spread over the liquid-liquid interface effectively decreasing the interfacial tension. In this case, the equilibrium structural characteristics, such as shape and size, of nanogel particles are determined by a range of factors

including interfacial tension between the two liquids, particle elasticity, and affinity of the nanogel polymer to either liquid phase. An extent of deformation and an effective depth of protrusion of microgels into each of the two liquid phases depends on the affinity between the polymer strands and each of these phases^{4, 15, 16}. The interfacial tension between the two liquid phases also significantly affects the microgels spreading, with higher extent of spreading observed for higher interfacial tension¹⁷. Softer nanogels spread to a greater extent over a liquid-liquid interface compared to more densely crosslinked nanogels and hence provide better emulsion stability⁵. Further, the spreading of the microgels and nanogels can be controlled dynamically via a range of external stimuli¹⁰, making these particles excellent candidates for emulsion stabilizers to form Pickering emulsions^{5, 18}. Similar to the microgels in a single solvent, a volume phase transition can be triggered in thermoresponsive or pH-responsive gel particles adsorbed at the interfaces resulting in a reduced interfacial coverage due to particle collapse and a subsequent loss of emulsion stability^{10, 19}.

Herein, we characterize controlled degradation of a nanogel particle in a single solvent and at the liquid-liquid interface. Controlled degradation is of interest since it can be used to dynamically tailor size, shape and thereby transport properties of nanogels and microgels in various environments. In particular, photo-triggered degradation can be turned on and off remotely, which could bring further advantages to regulate properties of these soft particles and rates of cargo release from these nano- and microcarriers. For the nanogels adsorbed at the liquid-liquid interfaces, controlled degradation could provide means to dynamically tune properties of these interfaces, such as interfacial tension and topography of a liquid-liquid

interface. Unlike rather comprehensive understanding of gelation processes for various polymer systems, understanding of the process of network degradation to date remains limited. Controlled degradation can be introduced in micro and nanogels via several pathways²⁰. Previous experimental studies provide insights into the erosion of the microgels with chemically labile crosslinkers^{21, 22} and microgels with blocks degradable via hydrolysis of ester bonds²³. Progress of microgel degradation in experiments has been tracked via measurement of the size of microgel particles either in suspensions^{1, 23, 24} or adsorbed on a solid substrate^{21, 22}. Measurements in suspension show distinctly different profiles for microgels with homogenous network architecture compared to microgels with an initial core-shell structure²⁴. The measurements at the surface are either performed by direct observation of degradation of microgel particles adsorbed on a solid substrate²¹ or by extracting the nanogel particles from the degrading medium and then depositing them on a solid substrate for measurements and characterization²².

Since nanogels and microgels are soft polymer networks with characteristic linear sizes on the order of tens to hundreds nanometers to tens of microns, respectively, mesoscale modeling approaches are commonly used to capture their behavior in solvents and at the interfaces. Dissipative Particle Dynamics (DPD)²⁵⁻²⁷, a mesoscale approach that has been used for modeling a broad range of multi-component systems²⁷⁻⁴², is often chosen to model behavior of microgels at liquid-liquid interfaces^{4, 15, 19, 43-47}. To model controlled degradation and erosion in hydrogels, we recently adapted a modified segmental repulsive potential (mSRP)⁴⁸ to overcome unphysical crossing of polymer chains along with modeling degradable bonds^{49, 50}.

As a model polymer network, we focused on gels synthesized by the end-linking of four-arm polyethylene glycol (PEG) precursors⁵¹⁻⁵³ originally fabricated by Sakai et al⁵³. These precursors can be modified during their synthesis by including photodegradable functional groups, for example nitrobenzyl⁵⁴⁻⁵⁶ or coumarin^{51, 54} groups. We showed⁴⁹ that the reverse gel point characterizing disappearance of the percolated network is close to but somewhat higher than the value predicted by the bond percolation theory on a diamond lattice^{57, 58}. In what follows, we use the same model polymer network with controllably degradable crosslinks between four-arm polymer precursors⁴⁹ and focus on characterization of structural characteristics of the remnant nanogel and distribution of broken-off fragments during the degradation process. We consider degradation of nanogels in a single solvent and at the liquid-liquid interface. We show that the affinity between the polymer and solvent strongly affects the evolution of shape and size of the remnant nanogel during the degradation process.

Methods

First we outline the DPD formulation used in this work, further details of this methodology and most recent developments can be found in the original publications^{25, 26, 59} and in the recent reviews^{27, 28}, respectively. Within the DPD approach, groups of atoms are coarse-grained into beads, with their motion being governed by the Newton's equations of motion²⁶:

$$\frac{d\mathbf{r}_i}{dt} = \mathbf{v}_i, \frac{d\mathbf{p}_i}{dt} = \mathbf{F}_i, \tag{1}$$

where r_i , v_i , and $p_i = mv_i$ are the position, velocity, and momentum of the bead i of mass m, and F_i is total force acting on this bead. For the non-bonded beads, this force encompasses three contributions, $F_i = \sum (F_{ij}^C + F_{ij}^D + F_{ij}^R)$, with the summation being taken over all other beads $(j \neq i)$ within a cut-off distance r_c , and F_{ij}^C , F_{ij}^D , and F_{ij}^R representing conservative, dissipative, and random forces, respectively²⁶. We use the most common choice of the conservative force^{26,59}:

$$\mathbf{F}_{ij}^{c} = \begin{cases} a_{ij} \left(1 - r_{ij} / r_c \right) \mathbf{e}_{ij} & \left(r_{ij} \le r_c \right) \\ 0 & \left(r_{ij} > r_c \right) \end{cases}$$
 (2)

which corresponds to soft repulsive potential, where the maximum repulsion between the beads i and j is defined by the interaction parameter a_{ij} , $r_{ij} = |r_{ij}|$ is the distance between these beads, $r_{ij} = r_i - r_j$, and $e_{ij} = r_{ij}/r_{ij}$ is the unit vector between the centers of these beads. We set the bead number density to three with r_c , temperature, and mass of each bead set to 1.0 in reduced DPD units^{25,26}. For the beads of the same type, the repulsion parameter is chosen as $a_{ii} = 78.0$ (here and below, the a_{ij} values are provided in the reduced DPD units²⁶, $\frac{k_B T}{r_c}$). This choice corresponds to the three water molecules coarse-grained into a single DPD bead with $r_c = 1$ in reduced DPD units related to the dimensional value of $r_c \approx 0.65$ nm. This mapping was originally derived by Groot and Rabone to model lipid bilayers with each DPD bead incorporating three carbons. It is worth noting that higher degrees of coarse-graining can also be used in DPD simulations; for example, DPD parametrization of polymer chains containing hydrophilic (oxyethylene) and hydrophobic fragments was detailed by Lee et al61 for a range of parametrization of DPD bead sizes (ranging from 3 to 6 water molecules per

bead). For the parameter choice introduced above (three water molecules coarse-grained into a single DPD bead), one hydrophilic bead was taken to represent⁶¹ 1.5 CH₂OCH₂ groups and one hydrophobic bead represented three CH₂ groups, same as in Ref. ⁶⁰. Herein we use the same mapping of DPD beads^{60, 61}, so that one bead of the PEG polymer strand composing nanogel represents 1.5 CH₂OCH₂ groups and one oil bead represents three CH₂ groups.

The interaction parameter between the beads of different types is chosen based on the affinity between the respective moieties as $a_{ij} = a_{ii} + 3.27\chi_{ij}$, where χ_{ij} is the Flory-Huggins interaction parameter. The repulsion parameter between the polymer and water beads is chosen based on the PEG-water Flory-Huggins interaction parameter⁶², $\chi = 0.45$, as $a_{pw} = 79.5$, and the repulsion parameter between the polymer and oil beads is chosen as $a_{po}=85.0.$ Both these values are close to the values chosen in Ref. 60 to capture the interactions between polyethyleneoxide and water beads and polyethyleneoxide and oil beads (where one DPD bead represents three CH2 groups), respectively. For simplicity, the degradable end groups are taken to have the same solubility as PEG beads. We vary the repulsion parameter between the water and oil phase in the studies below by setting $a_{ow} =$ 100, $a_{ow} = 120$, and $a_{ow} = 150$ in selected series of simulations; note that an increase in a_{ow} corresponds to an increase in the interfacial tension between the oil and water phases²⁶. Within the range of chosen values of a_{ow} , the oil phase is immiscible with water; it had been previously shown in DPD simulations by Nair et al 63 that the dependence of a mean square radius of gyration on the degree of polymerization of chains composed of oil beads with $a_{ow} =$

100 follows an anticipated scaling for poor solvent. The specific choice of the repulsion parameters in each simulation series below along with the system sizes is provided in Tables S1 and S2 of the Supplementary Information.

The remaining two contributions to the total force between the non-bonded beads, dissipative and random forces, read²⁶: $\mathbf{F}_{ij}^D = -\gamma \omega_D(r_{ij})(\mathbf{e}_{ij} \cdot \mathbf{v}_{ij})\mathbf{e}_{ij}$ and $\mathbf{F}_{ij}^R = \sigma \omega_R(r_{ij})\zeta_{ij}$. $\Delta t^{-0.5} m{e}_{ij}$; here, γ and σ are the strengths of these forces, $m{v}_{ij} = \mbox{ } m{v}_i - \mbox{ } m{v}_j$ is the relative velocity, Δt is the simulation time step, and ζ_{ij} is symmetric Gaussian random variable with zero mean and unit variance. The following conditions are imposed to satisfy the fluctuation-dissipation theorem: $^{26,59}\sigma = \sqrt{2\gamma k_B T} = 3$ and $\omega_D(r_{ij}) = \omega_R^2(r_{ij})$. We chose the weight functions in the same form as the conservative force²⁶, $\omega^R(r_{ij}) = 1 - \frac{r_{ij}}{r_c}$, for $r_{ij} < r_c$ and zero otherwise; while this is the most common choice, other choices are also permitted⁶⁴ as long as the above conditions ensuring fluctuation-dissipation theorem are satisfied. The time step is set at $\Delta t =$ 0.02τ ; relating reduced DPD unit of time to the respective dimensional value can be done via matching the diffusion coefficient of water beads as⁶⁰ $\tau \approx 88$ ps. Unless stated otherwise, all quantities in this work are provided in reduced DPD units, with r_c as the unit length, τ as the unit time, and k_BT as the unit of energy.

For the bonded beads an additional force is introduced in eq. (1) corresponding to the harmonic potential, $U_{bond} = \frac{\kappa_b}{2} (r_{ij} - r_b)^2$, where we set⁴⁹ $K_b = 10^3$ as a spring constant and $r_b = 0.7$ as an equilibrium bond distance. To prevent unphysical crossing of polymer chains, we also adopted modified segmental repulsion potential (mSRP)⁴⁸ DPD formulation. In mSRP

DPD, a force acting between the centers of the bonds separated by a distance $d_{ij} = |\boldsymbol{d}_{ij}|$ below the cutoff distance d_c , is introduced as ⁴⁸:

$$\boldsymbol{F}_{ij}^{mSRP} = \begin{cases} b \left(1 - \frac{d_{ij}}{d_c} \right) \boldsymbol{e}_{ij}^S & (d_{ij} < d_c) \\ 0 & (d_{ij} \ge d_c)' \end{cases}$$
 (3)

where $e_{ij}^S = \frac{d_{ij}}{d_{ij}}$. We set b=80 as the maximum strength of the mSRP repulsion and $d_c=0.8$ as the mSRP cut-off distance; these values were shown to effectively minimize topology violations in the original framework⁴⁸ and in the subsequent studies⁴⁹. The LAMMPS simulation package ^{65, 66} along with the mSRP code⁴⁸ was used to integrate the equations of motion; and Visual Molecular Dynamics software⁶⁷ was used to perform all visualizations reported in this work.

To simulate bond breaking within the nanogel particles, random numbers are generated for each degradable bond at each reaction time, τ_r , which is taken ten times larger than the time for each update of positions of the beads⁶⁸⁻⁷², $\tau_r = 10\Delta t$. The bond is broken if the generated random number is lower than the probability of bond breaking, P. After a bond breaking event occurs, the two beads remain unbonded for the rest of the simulation with no change to the interaction parameters of these beads. Similar stochastic approaches have been used previously for various reactive systems⁷¹⁻⁷⁴. Using this approach the fraction of degradable bonds intact at a given time, p(t), accurately follows first order degradation kinetics, $p = \exp(-kt)$, with the rate constant⁵⁰ $k = P/\tau_t$. For various polymer networks undergoing controlled photodegradation, the degradation occurs⁷¹ orders of magnitude slower than the characteristic diffusion times on the relevant length scales^{49,50}. Hence we use relatively low

degradation rate set by⁴⁹ $P = 9 \cdot 10^{-6}$ (corresponding to degradation rate of $k = 4.5 \times 10^{-5} \tau^{-1}$) to ensure that our system is in a kinetically limited regime^{50,71}. It should also be noted that although bond breaking can take place every ten timesteps, we only store the bead trajectories every $t_M = 1000\Delta t$ to decrease file sizes with minimal loss of information. We use our recently implemented modification of the mSRP framework which allows for the additional mSRP forces to be switched off as the bonds break^{49, 50}; this modification is implemented within the LAMMPS simulation package as pair style srp/react⁷⁵.

The diamond-like lattice^{71,76} is used as an initial configuration of the nanogel's polymer network. An effective "unit cell" is created by first placing tetra-functional beads at lattice sites and then placing $N_x/2$ beads for each of the four polymer arms⁴⁹, so that there are N_x beads between the centers of two bonded precursors. To create nanogel particles, we first replicate this unit cell N_{rep} times in each of the x, y, and z directions. The fractional precursors with a functionality less than four at the faces of the initially cubic network are deleted and a sphere is drawn inside the cubic network with its center as the center of the cube and a diameter (D_{cut}) smaller than the side length of the cube. All precursors with any bead outside of the sphere are deleted to generate approximately spherical nanogel particle with an integer number of total precursors N_p and with dangling chains at the surface of the network⁵⁰. All the parameters used for constructing the initial network are provided in Table S1. Prior to the production runs, all the nanogels are equilibrated in the water phase for $12x10^5$ time steps without allowing for degradation. An equilibrated nanogel particle swollen in water is shown

in Fig. 1b. PEG beads are shown in cyan, and the end groups of both precursors are shown in red and blue, respectively. For clarity of representation, the water beads are hidden. The degradable bonds in the system are chosen to be the bonds between the end functionalities (Fig. 1a) since the cleavable sites are typically chosen to be in the proximity of the end functionality^{51,58}. Three water molecules are represented by a single DPD bead, the oil phase is modeled using short chains with four beads each⁶³, and the number of beads between the centers of two bonded precursors, N_x , is varied as detailed in Table S1.

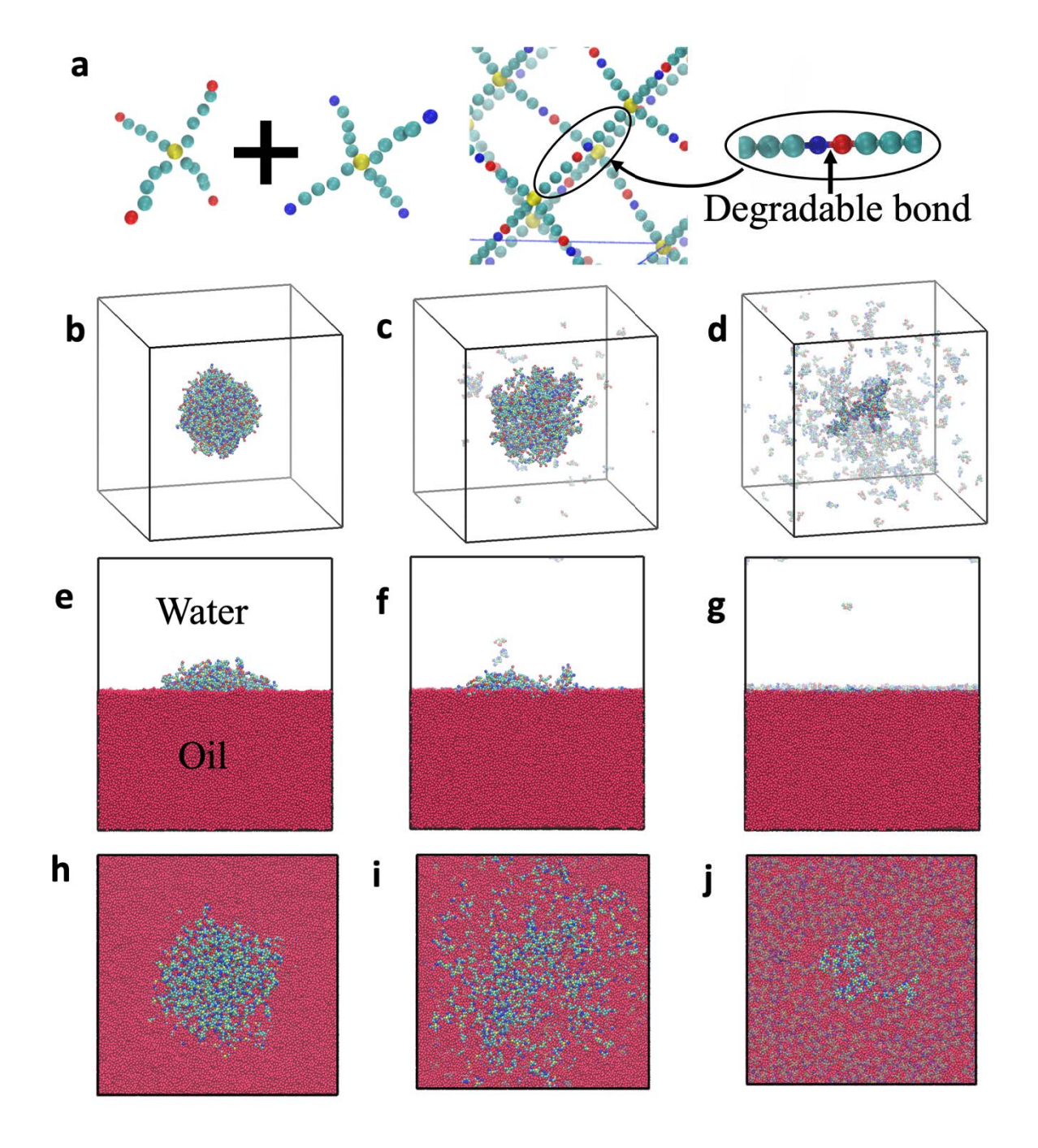


Figure 1. Nanogel degradation in water and at the oil-water interface. (a) Schematic of the fragment of nanogel network with degradable bonds. Snapshots of a single nanogel corresponding to the reference parameter set (set F in Table S1), **(b-d)** nanogel degradation in good solvent and **(e-j)** degradation of a nanogel initially adsorbed at the oil-water interface.

Dimensionless time, in units of τ , is t=0 in (b, e, h), t=10,000 in (c, f, i), and t=22,000 in (d, g, j). Polymer beads are colored as described in the text, oil beads are shown in red and water beads are hidden for visual clarity. (e-g) Side view and (h-j) top view of the nanogel at the interface. In the above snapshots, the largest cluster is highlighted while all other polymer beads shown as translucent.

The processes of degradation of nanogels in a single solvent and degradation of nanogels adsorbed at the liquid-liquid interface are characterized and compared in this study. In all the simulations of the gel particles degrading in a single solvent, bond breaking is switched on immediately after the equilibration step and the degradation is carried on for $3x10^6$ time steps. In all the simulations involving degradation of the nanogels at the liquid-liquid interface, the nanogels equilibrated in water are first placed into the water phase in the binary oil-water system and are allowed to adsorb onto the interface and attain a new equilibrium shape. The degradation is turned on only after the gels are equilibrated at the liquid-liquid interface; then the degradation study is carried out for $3x10^6$ time steps.

Results and Discussion

Characterizing nanogel degradation in bulk and at the liquid-liquid interface

We first characterize degradation of a nanogel depending on its environment via tracking and comparing the main characteristics of the degradation process for the same nanogel particle swollen in a good solvent and adsorbed at the liquid-liquid interface. The

snapshots during degradation are shown in Fig. 1 with panels b-d corresponding to degradation in water and panels e-j corresponding to degradation at the oil-water interface. The parameters are chosen corresponding to the reference parameter sets (Tables S1 and S2). Prior to the onset of degradation, the nanogel swollen in water attained approximately spherical shape upon equilibration (Fig. 1b). During degradation, the breaking of bonds results in an effective decrease in crosslink density accompanied by detachment of fragments from the nanogel particle. To characterize the degradation process, we first define a cluster as a set of bonded precursors at any stage during the degradation⁴⁹. In a similar manner, we define the nanogel as the largest cluster of bonded precursors at a given time instant. This definition is relevant until the reverse gel point, since only until this point the largest cluster represents the remnant part of the original nanogel, as can be seen in Fig. S1. The largest cluster of chemically bonded precursors is highlighted in all images in Fig. 1, while the detached fragments are shown as translucent. The decrease in the effective crosslink density is pronounced at relatively early times, during which approximately homogenous swelling of the remnant nanogel in water is observed (Fig. 1c, also see quantitative characterization below). At this stage, a fraction of the fragments that are detached from the nanogel diffuses away from the network while some fragments remain stuck inside the particle. At late times, due to detachment of sufficiently large fraction of fragments, the nanogel loses its spherical shape.

In comparison to the nanogel in the water (Fig. 1, top row), the nanogel at the liquidliquid interface has an initial asymmetric shape prior to the degradation (Fig. 1e,f). This shape is defined by the interplay between the energetically favorable shielding of oil-water contacts and an energy penalty due to the increase in elastic energy contribution upon nanogel deformation. Prior studies demonstrated effective flattening of gel particles at the interfaces^{5,} 11, 15 with more pronounced interfacial spreading of loosely crosslinked gels. The specific deformation and the depth of protrusion into each liquid phase depends on the affinity between the polymer strands and these liquids phases^{4, 15, 16}. For the chosen affinity of the polymer network with both liquid phases (see Model section), the nanogel adsorbed at the interface largely remains in the water attaining close to hemispherical shape prior to degradation. Similar to the nanogel in water considered above, at the beginning of degradation the decrease in crosslink density is notable and correspondingly leads to the enhanced spreading and interfacial coverage (Fig. 1f,i). The remnant nanogel particle along with most of the detached fragments remains adsorbed at the interface with the adsorbed fragments diffusing along the interface to promote shielding of a large number of unfavorable oil-water contacts. The fragments that detach while in the water phase are also later adsorbed by the interface (one such fragment is highlighted in Fig. 1f). Below we characterize the reverse gelation transition for the nanogels at the interface and that in a single solvent.

Characterizing nanogel size, shape, reverse gel point, and mass loss

Prior to the degradation the nanogel constitutes the only cluster in the system. During the degradation process, clusters of different sizes (i.e. both different numbers of precursors and different geometric sizes) and shapes are formed in the system. The nanogel particle,

defined above as the largest cluster of connected precursors, contains N(t) precursors at any time, out of the initial N_p precursors in the original nanogel. We measure the size and shape of the degrading remnant nanogels via the gyration tensor of the largest cluster at any time. The components of the gyration tensor are given as $S_{mn} = \frac{1}{N_b^2} \sum_{i=1}^{N_b} \sum_{j=i}^{N_b} (r_m^i - r_m^j) (r_n^i - r_n^j)$, where m,n indicate cartesian directions, N_b is the total number of beads comprising the nanogel and r_m^i is the m-th component of the position vector \mathbf{r}^i of the t^h particle. The eigenvalues of the gyration tensor, λ_1, λ_2 , and λ_3 , provide a measure of characteristic size squared along three principle directions and allow one to calculate the radius of gyration, R_g , and the shape anisotropy, κ^2 , as:

$$R_g^2 = \lambda_1 + \lambda_2 + \lambda_3 \tag{4}$$

and

$$\kappa^2 = \frac{3(\lambda_1^2 + \lambda_2^2 + \lambda_3^2)}{2(\lambda_1 + \lambda_2 + \lambda_3)^2} - \frac{1}{2}.$$
 (5)

The κ^2 is typically used to characterize shapes of various polymeric species⁷⁷⁻⁷⁹ and ranges from $\kappa^2=0$ for an ideal sphere to $\kappa^2=0.25$ for a planar object (with $\lambda_1=\lambda_2$ and $\lambda_3=0$) to $\kappa^2=1$ for points on a line⁷⁷. For linear polymer chains, $\kappa^2\approx0.43$ and $\kappa^2\approx0.39$ in good and theta solvents, respectively ⁸⁰⁻⁸².

The time evolution of R_g and κ^2 for a nanogel particle (reference parameter set F in Table S1) degrading in water (black curve) and at the interface (red curve) is provided in Fig. 2a,b. The values at t=0 indicate the equilibrium values prior to degradation. As degradation begins, the R_g of the nanogel in the water increases approximately up to $t\approx 19{,}000$ for the

chosen simulation run (Fig. 2) and then decreases. During the initial increase in R_g , up to $t \approx$ 10,000, there is no significant change in κ^2 . Close to zero values of κ^2 correspond to the equilibrium spherical nanogel shape prior to and during initial stages of degradation. Hence, the nanogel size initially increases without any notable increase in shape anisotropy; this indicates that the nanogel undergoes approximately homogenous swelling maintaining the spherical shape during this initial phase of degradation. The second portion of the increase in R_g is somewhat less smooth (at times approximately within the interval $t \in [10^4 : 1.9 \cdot 10^4]$ for the simulation in Figure 2); during this time frame, some increase in κ^2 is observed, indicating notable deviations from spherical symmetry. The latter sharp decrease in R_g is accompanied by a significant increase in the shape anisotropy. As we show below, this decrease in R_g and increase in κ^2 correspond to the reverse gelation transition. At late times the measured value of R_g and κ^2 correspond merely to the largest polymeric cluster in the system and not to the remnant nanogel (as discussed in Fig. S1). Thus at late times the value of R_g decreases significantly while κ^2 fluctuates around an average value of $\kappa^2 \approx 0.40 \pm 0.19$ (Fig. 1b, the average is taken at time interval $t \in [35000:50000]$ using 150 frames). Large fluctuations of the shape anisotropy were previously reported while characterizing conformations of polymers of various architectures^{78, 80-82}.

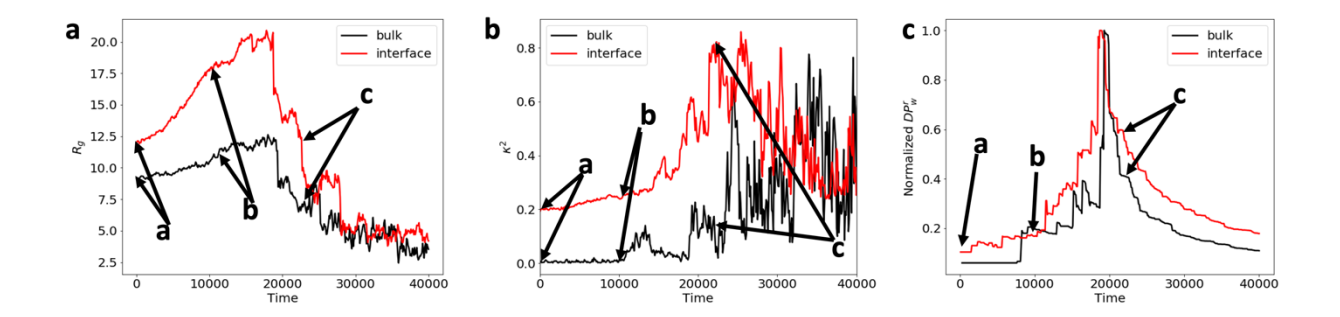


Figure 2. Time evolution of (a) the radius of gyration, R_g , (b) shape anisotropy, κ^2 , (c) reduced weight average degree of polymerization, DP_w^r . The points marked by arrows correspond to the snapshots in Figure 1. The data in **c** are normalized by the corresponding maxima.

For the nanogel at the interface, the initial values of both R_g and κ^2 are higher than the values for the nanogel in water due to the initial spreading of the nanogel at the interface prior to degradation as discussed above. As degradation begins, the R_g increases faster compared to the nanogel in water and then decreases sharply at late times ($t > \approx 18,000$ for the simulation in Fig. 2). In contrast to the degradation in water, κ^2 for the degradation at interface increases continuously from the beginning of degradation. This indicates that the nanogel loses its initial shape at the interface immediately after the onset of degradation since the degradation promotes the spreading over the interface.

Next we relate the observed trends in R_g and κ^2 to the reverse gelation transition in both cases of degradation in a single solvent and degradation at an interface. Analogous to the approach used to identify gel point in the simulations of gelation process⁸³⁻⁸⁶, the location of the reverse gel point can be identified⁴⁹ using the reduced weight average degree of polymerization, DP_w^r , defined as

$$DP_{w}^{r}(t) = \frac{\Sigma' n_{i}(t) i^{2}}{\Sigma' n_{i}(t) i'}, \tag{6}$$

where $n_i(t)$ is the number of topological clusters with size i at time t and the 'indicates summation over all but the largest cluster. The DP_w^r curves for the degradation of a nanogel in water (in black) and at the interface (in red) are shown in Fig. 2c. The critical time instant corresponding to the peak value of DP_w^r indicates the reverse gel point⁴⁹, which is analogous to the definition of gel point in gelation simulations⁸³⁻⁸⁸. The time instant corresponding to peaks in DP_w^r in Fig. 2c, t_c , allows one to identify a reverse gel point as a critical value of the fraction of degradable bonds intact at this time instant⁴⁹, $p_c = \exp(-kt_c)$. The exact location of the reverse gel point somewhat differs for the individual simulations due to the stochastic nature of the degradation process (Fig. S2). Indeed, the reverse gel points are approximately within the error bars for the two scenarios when averaged over five independent simulation runs. Specifically, $p_c = 0.44 \pm 0.01$ for the degradation in water and $p_c = 0.47 \pm 0.05$ for the degradation at interface. This is expected since the current model assumes, for simplicity, no effect of the surrounding moieties on the probability of bond breaking. Once the reverse gel point for a given system is identified, the proximity to this point at a given time instance can be defined via the relative extent of degradation⁴⁹, ϵ , which is analogous to the definitions of relative extent of gelation during the gelation process⁸⁹, as:

$$\epsilon = \frac{p_c - p}{1 - p_c}.\tag{7}$$

Note that the fraction of bonds broken, 1 - p, defines an extent of the degradation reaction and hence the definition of ϵ above provides a relative measure of proximity to the reverse gel

point. With the above definition, $\epsilon=-1$ corresponds to the onset of degradation, $\epsilon=0$ to the reverse gel point, and positive values of ϵ correspond to the degradation after the reverse gelation transition. In what follows, we plot all data characterizing degradation processes as a function of ϵ to identify main trends in evolution with the proximity to the reverse gel point.

The dependence of shape anisotropy κ^2 , the ratio of the largest to smallest eigenvalues λ_1/λ_3 , and R_g for nanogels degrading in water (black curves) and for nanogels degrading at the interface (red curves) with an increase in the extent of degradation up to the reverse gel point is provided in Fig. 3. The values in this and following plots are averaged over five independent simulations with error bars denoting standard deviation. Relatively far from the reverse gel point ($\epsilon \approx$ [-1:-0.38]), $\kappa^2 \approx$ 0 and $\lambda_1/\lambda_3 \approx$ 1 for the degradation in water with relatively small error bars (Fig. 3a,b), confirming that the broken bonds at this extent of degradation result in an effective decrease of the crosslink density and nearly isotropic swelling of the nanogel particle. Correspondingly, R_g increases monotonically with relatively small error bars at these low ϵ (Fig. 3c). With further increase in the extent of degradation of nanogel in water ($\epsilon \gtrsim -0.38$), both κ^2 and λ_1/λ_3 somewhat increase with notably larger error bars indicating that nanogel is no longer isotropic. However, the average value of κ^2 and the standard deviation around mean remain low with respect to that expected for example for a random coil configuration.

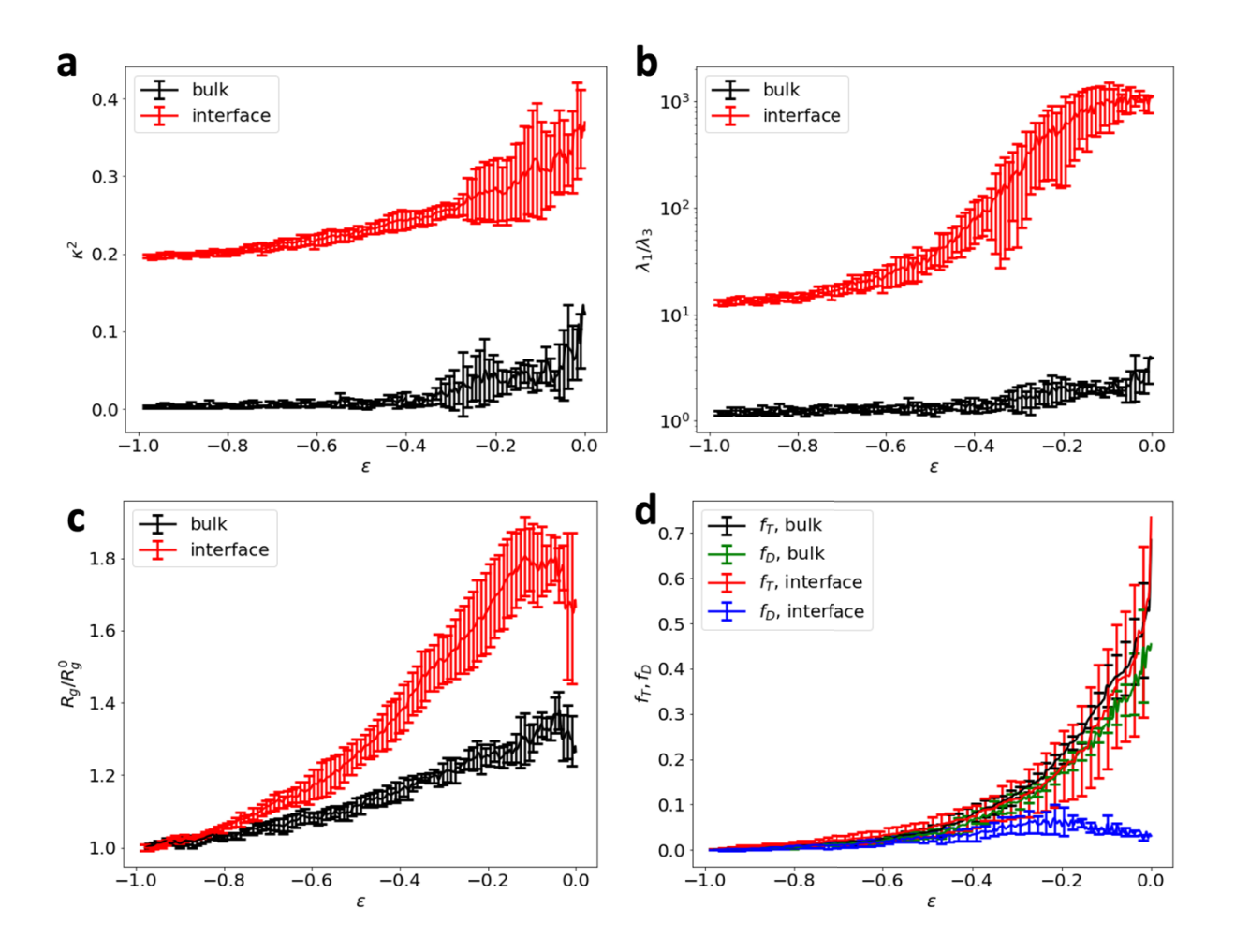


Figure 3. Evolution of (**a**) shape anisotropy, (**b**) ratio of largest to smallest eigenvalues, (**c**) radius of gyration normalized by the value prior to degradation, and (**d**) topological and distance-based mass loss for degradation in water and at the interface. The distance-based mass loss is represented by green (water) and blue (interface) curves, and f_T is shown in black (water) and in blue (interface). All data represent an average over five independent simulations with error bars denoting standard deviation.

On the contrary, both κ^2 and λ_1/λ_3 increase nearly monotonically from the onset of degradation with the increase in ϵ for the gels degrading at the interface (red curves in Fig. 3a,b). Note that the initial values of κ^2 and λ_1/λ_3 on these plots are defined by the equilibrium

shape of the gel particle adsorbed at the interface. As discussed above, this shape is anisotropic and depends on the affinities between all the moieties in the system and on the crosslink density of the nanoparticle prior to degradation. A distinct (over two orders of magnitude) increase in the ratio λ_1/λ_3 with an increase in ϵ indicates that the nanogel essentially spreads over the interface during the degradation. Correspondingly, more distinct increase in the radius of gyration normalized by that prior to degradation is observed with an increase in ϵ for the nanogels in water (Fig. 3c).

The characterization of topological clusters described above provides information about the remnant nanogel particle and allows one to identify the reverse gel point. In addition, it is also instructive to analyze the spatial distribution of fragments detaching from the degrading nanogels. Hence, in addition to the characterization of topological clusters discussed above, we also define a distance-based cluster or an agglomerate as the set of polymer precursors each having at least one contact with another precursor⁴⁹ (two beads belonging to these precursors are within the interaction distance r_c). Correspondingly, during the degradation process we calculate the number of precursors in the largest agglomerate in the system, $N_D(\epsilon)$, along with the size of the largest topological cluster as defined above, $N(\epsilon)$. At the onset of degradation, $N_D(-1) \equiv N(-1) \equiv N_p$. During the degradation, $N_D(\epsilon)$ can significantly exceed $N(\epsilon)$ since it accounts for the fragments stuck within or remaining in the close proximity to the surface of the largest topological cluster. The fraction of precursors broken-off from the nanogel can be characterized via the topological mass loss, $f_T(\epsilon) = 1 - N(\epsilon)/N_p$, while the fraction of

precursors that not only broke-off but also diffused away (to distance exceeding r_c) from the largest agglomerate (which encompasses the remnant nanogel) can be characterized via distance-based mass loss as $f_D(\epsilon) = 1 - N_D(\epsilon)/N_p$.

The fraction of broken-off fragments represented by $f_T(\epsilon)$ is indistinguishable for degradation in water and at an interface (black and red curves in Fig. 3d). This is anticipated, since topological mass loss is defined by the rate constant of bonds breaking and does not depend on diffusion of broken-off fragments. For degradation in water, f_D in this reference scenario (green curve) is indistinguishable from f_T , clearly indicating that no fragments are stuck within the largest agglomerate or in close proximity to it. On the contrary, f_D at the interface remains close to zero (blue curve in Fig. 3d) as the fragments that detach from the nanogel remain adsorbed at the interface. f_D somewhat increases around $\epsilon \approx -0.2$ as some fragments diffuse away from the nanogel particle, however at later times these fragments are adsorbed onto the interface. In the proximity of the reverse gel point, the degraded fragments cover the interface having contacts with largest agglomerate thereby reducing f_D to values close to zero.

Scaling of reverse gel point

Next we identify the reverse gel point as a function of the number of precursors in the nanogel, N_p . The specific nanogel parameters used in multiple series of simulations in water and at the interface are provided in Tables S1 and S2. For each parameter set the critical value

of p_c is found from the maximum of the reduced weight-average degree of polymerization using the procedure described above. The values of \bar{p}_c provided in Fig. 4 are averaged over five independent simulation runs with the error bars representing the standard deviation, $\Delta \bar{p}_c$.

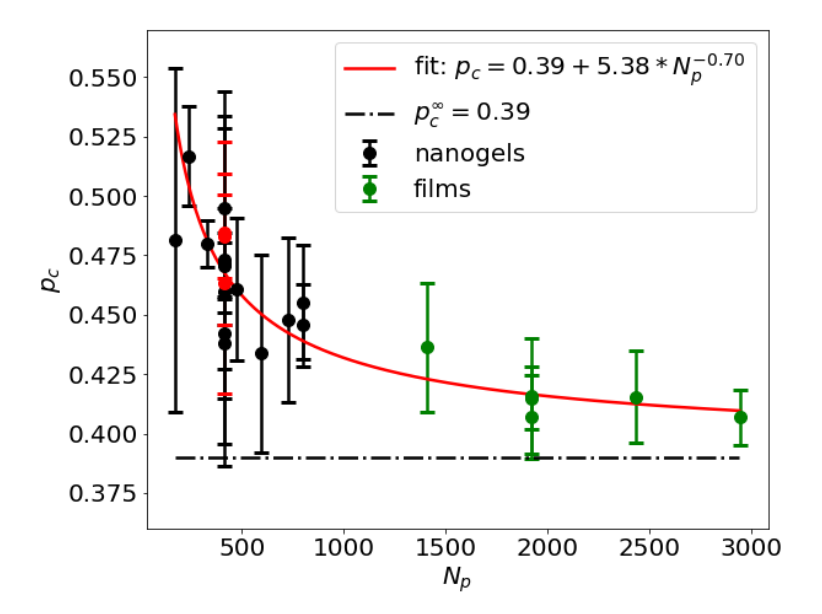


Figure 4. Scaling of the reverse gel point with the number of precursors, N_p . The dependence of reverse gel point p_c on the total number of precursors in the system. Symbols correspond to the measured p_c for nanogels degrading in water (black symbols), nanogels degrading at the interface (red symbols) and hydrogel films from Ref. ⁴⁹ (green symbols). The dashed line corresponds to $p_c^{\infty} = 0.39$. The error bars represent standard deviation taken over five independent simulations in each case. The red line corresponds to a weighted nonlinear least squares fitting of the simulated data.

The data from nanogels in water and at the interface are shown in Fig. 4 by the black and red symbols, respectively. The data points shown by the green symbols are reproduced from our

previous work on hydrogel films⁴⁹. The \bar{p}_c is lower for the simulations with higher total number of precursors and this value of reverse gel point is also close to the analytical estimate from the bond percolation theory on a diamond lattice^{57, 89} marked by the dashed line in Fig. 4. There is an evident increase in both \bar{p}_c and $\Delta \bar{p}_c$ with the decrease in N_p . The increase in $\Delta \bar{p}_c$ is attributed to the stochastic nature of the process since higher number of precursors provide better statistics. The increase in \bar{p}_c upon decrease of the number of precursors is anticipated from analytical theories of gelation reflecting the finiteness of any "simulated" system (finite number of precursors) compared to the infinite system sizes assumed in classical percolation theories^{57, 89, 90}. The following relation is expected to hold for percolation on regular lattices during gelation process^{57, 88, 89}:

$$p_c(N_p) = p_c^{\infty} + cN_p^{-\sigma},\tag{8}$$

where p_c^{∞} is an analytical estimate for the percolation threshold on an infinite lattice, σ is a scaling exponent and c is a proportionality constant. It should be noted here that nanogel particles indeed consist of a finite number of polymeric precursors and hence, as opposed to gelation of macroscopic samples, effects of finiteness should be taken into account. For the gelation process modeled as percolation on Bethe lattice of functionality four, the values $p_c^{\infty} = 0.33$ and $\sigma = 0.5$ had been derived^{57,89}. However, both these values are not expected to hold for gelation processes that differ significantly from the ideal Bethe lattice percolation model and for the corresponding reverse gelation processes. For example, values of p_c^{∞} significantly exceeding the predicted 0.33 (so-called delay in the gel point) have been reported in a number

of studies of gelation processes^{85, 87, 88, 91-94}; this delay is typically attributed to intramolecular reactions. The gel point values close to percolation threshold on the diamond lattice (0.39) have been reported for the gelation of tetra-arm PEG precursors near the overlap concentration^{95, 96}. Further, the scaling exponent $\sigma = 0.5$ is not expected to necessarily hold for the systems with defects such as loops^{86, 88} or for the systems with intramolecular reactions. The scaling relation in eq. 8 had been used^{86, 88} for prediction of true gel points using Kinetic Monte Carlo simulations; it had been shown that the predicted gel point is insensitive to the scaling exponent within the range $\sigma \approx 0.3 - 0.7$.

Unlike fairly comprehensive understanding of gelation processes for various systems, understanding of the kinetics of network degradation remains limited. Reverse gel points ranging between 0.43 and 0.48 for networks formed by the tetra-PEG precursors at various stochiometric ratios were reported by Li et. al. ⁵⁸; the authors concluded that the reverse gel points observed in their work are close to the predictions of percolation models on the diamond lattice. In our recent work⁴⁹ we demonstrated that the reverse gel point calculated during degradation of hydrogel films formed by the tetra-arm precursors is close to but somewhat higher than predictions of bond percolation theory on a diamond lattice⁵⁷.

To estimate the scaling of the reverse gel point with the number precursors, N_p , based on our simulation data, we used a weighted nonlinear least squares regression method 97 . Equation 8 was used as the prediction model with a weighted loss function taken as $\sum \left(\frac{p_c(N_p) - \overline{p_c}}{\Delta \overline{p_c}}\right)^2$, where $p_c(N_p)$ is the predicted value and the summation is taken over all the

available data points. The choice of $1/\Delta \bar{p_c}$ values as weights is made herein to bias the fitting towards data points with lower $\Delta \bar{p_c}$ since these points are measured with higher certainty⁹⁷. By setting⁵⁷ $p_c^{\infty} = 0.39$ and treating c and σ as the fitting parameters, we obtained the best fit as $c = 5.38 \pm 2.38$ and $\sigma = 0.7 \pm 0.07$. The best fit to the simulation data points is provided in Fig. 4 as $p_c = p_c^{\infty} + 5.38 * N_p^{-0.70}$ (red curve).

Effects of polymer-solvent interaction

We now focus on the effect of polymer-solvent interaction on the degradation and erosion kinetics of nanogel particles in a single solvent. We consider three values of the polymer-solvent interaction parameter: $a_{ps} = 79.5$, 82.0 and 85.0 with $a_{ps} = 79.5$ representing a good solvent and $a_{ps} = 82.0$, 85.0 representing decrease in solvent quality. The snapshots for degradation of nanogels for these three cases are shown in Fig. 1b-d, Fig. 5a-c and Fig. 5d-f, respectively.

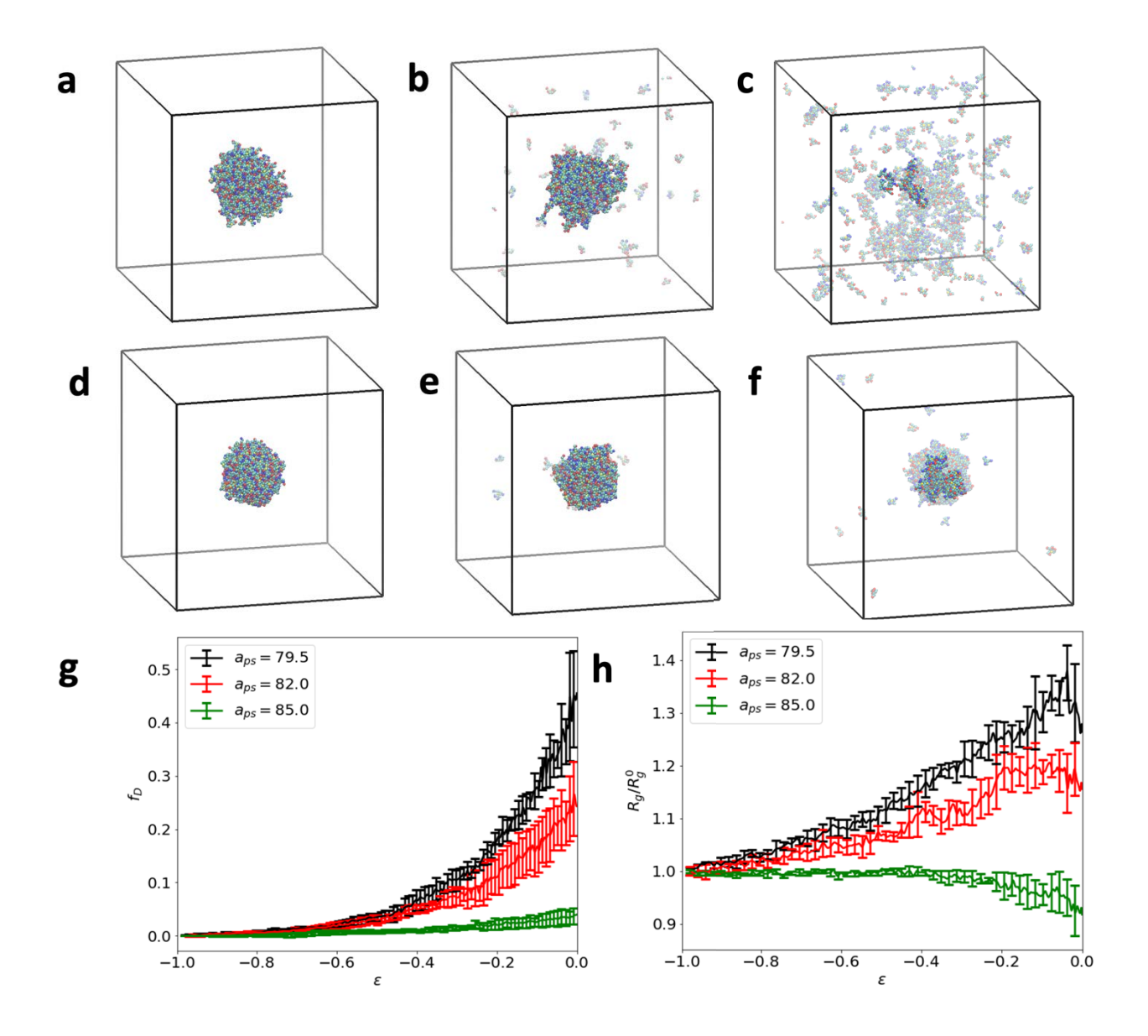


Figure 5. Effects of solvent quality on nanogel degradation in a single solvent. Snapshots of the nanogel degrading in a solvent with $a_{ps}=82.0$ (a-c) and in a solvent with $a_{ps}=85.0$ (d-i) at t=0 (a, d), t=10,000 (b, e) and t=22,000 (c, f). (g) Evolution of the distance-based mass loss and (h) radius of gyration during degradation in a solvent with $a_{ps}=79.5$ (black curve), $a_{ps}=82.0$ (red curve) and $a_{ps}=85.0$ (green curve).

A decrease in solvent quality results in a lower degree of swelling both prior to and during the degradation of the nanogel. This is evident in the initial and early time snapshots of the degrading nanogel particles. As expected, the topological mass loss, $f_T(\epsilon)$, in all three cases remains the same (Fig S4a). The fractional mass loss from the largest agglomerate, however, $f_D(\epsilon)$, follows distinctly different trends depending on solvent quality. Recall that f_D effectively accounts for the fragments that not only break-off but also diffuse away from the nanogel. For the solvent of intermediate quality ($a_{ps} = 82.0$, top row in Fig. 5), significantly smaller number of fragments are seen leaving the main agglomerate than that in the reference scenario at the same time instants (Fig. 1, top row). These differences are even more pronounced for the relatively poor solvent ($a_{ps} = 85.0$), where only small fraction of fragments is seen leaving the nanoparticle (second row in Fig. 5). As discussed above, no notable agglomeration of the broken-off fragments within the nanogel is observed for the good solvent case (black curve in Fig. 5g). Clearly some agglomeration of the broken-off segments within the largest agglomerate is observed for the intermediate solvent quality ($a_{ps} = 82.0$), resulting in significantly lower values of $f_D(\epsilon)$, in particular in the proximity of the reverse gel point (red curve in Fig. 5g). For the relatively poor solvent ($a_{pw} = 85.0$, green curve in Fig. 5g), the distance-based mass loss remains close to zero throughout the degradation indicating that almost the entire mass remains agglomerated with the largest agglomerate. This is also apparent from the snapshots in Fig. 5e-f, which show that majority of broken-off fragments

remain aggregated in the close proximity to the nanogel particle (for example, in Fig. 5f only the highlighted part in the center of the agglomerate is the nanogel particle).

Understanding fractional mass loss from the largest agglomerate in solvents of various qualities allows one to understand dependence of the radius of gyration of the nanogel degrading in these solvents as a function of the extent of degradation reaction. At the onset of degradation ($\epsilon = -1$), the radius of gyration depends on the equilibrium degree of swelling in the solvent of a chosen quality and as anticipated decreases with the decrease in solvent quality (Fig. S3b). To characterize a relative change in the radius of gyration depending on solvent quality, we plot the dependence of R_g scaled by the initial value of R_g for each case as a function of the proximity to the reverse gel point (Fig. 5h). As degradation occurs the nanogel in good solvent shows the highest relative increase in R_g (black curve in Fig. 5h). As discussed above, an effective decrease in the crosslink density enables higher absorption of water within the polymer network and thus an increased swelling of the nanogel is observed in a good solvent. For the gel degrading in solvent of relatively poor quality ($a_{ps}=85.0$, green curve in Fig. 5h), the R_q remains nearly constant until relative extent of degradation reaches about $\epsilon \approx$ -0.4; this is consistent with the above observation that up to this point there is essentially no mass loss from the largest agglomerate (green curve in Fig. 5g). Further increase in ϵ upon approaching reverse gel point results in the decrease in R_g , which is consistent with mass loss due to the fragments diffusing away from the nanogel as seen in Fig. 5g. Intermediate solvent quality ($a_{ps} = 82$, red curve in Fig. 5h) still leads to the swelling of the gel particle due to the

decrease in crosslink density, however the relative increase in ${\cal R}_g$ is less pronounced than that in the good solvent case.

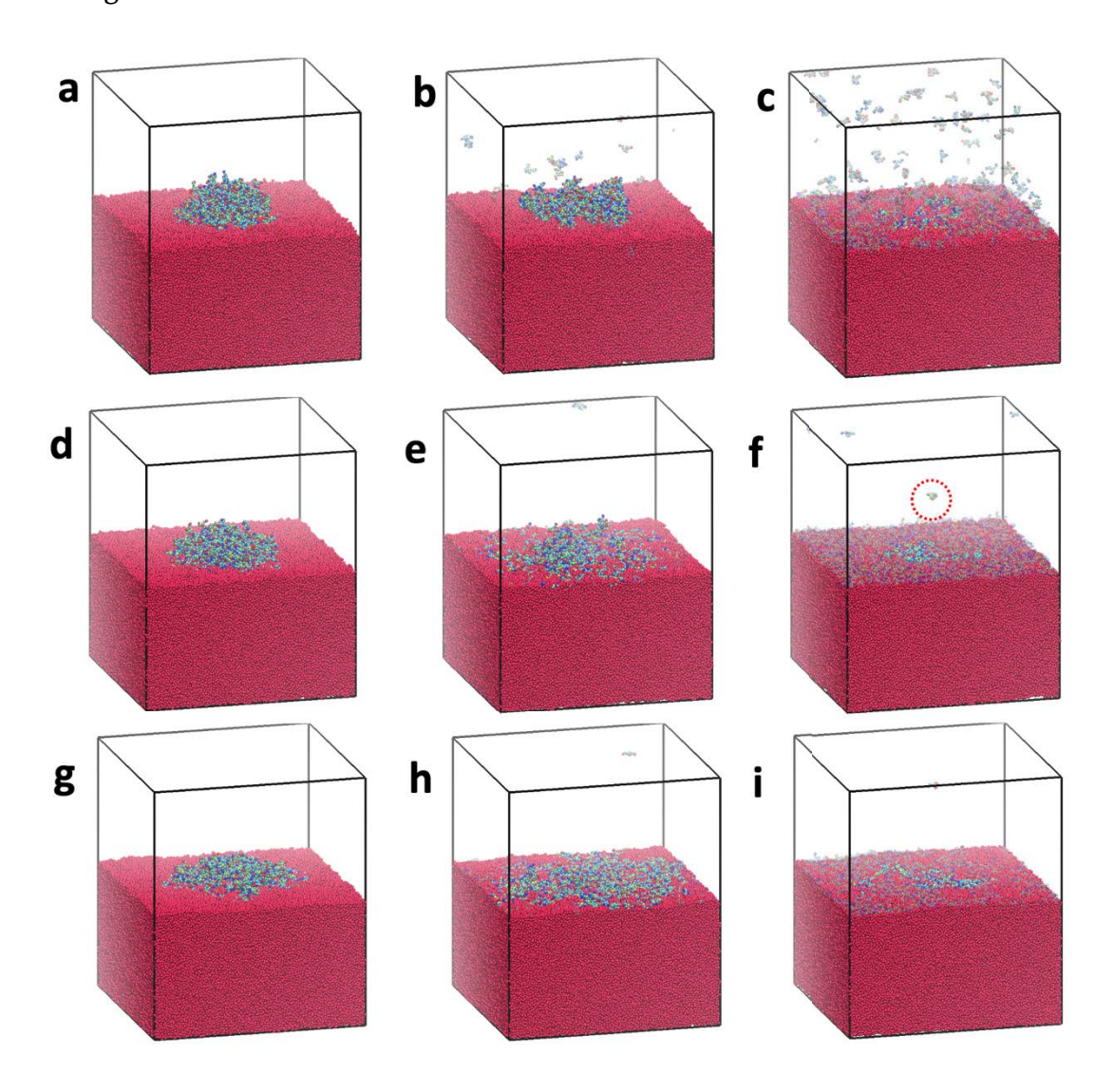


Figure 6. Snapshots of the nanogel degrading at an interface with the oil-water interaction parameter (a-c) $a_{ow} = 100$, (d-f) $a_{ow} = 120$ and (g-i) $a_{ow} = 150$ at (a, d, g) t=0, (b, e, h) t=10,000 and (c, f, i) t=22,000.

Similar to the effect of solvent quality in case of degradation in a single solvent, the interaction between the two liquids affects the kinetics of erosion and spreading of nanogel at the liquid-liquid interface. As introduced in the model section, we consider three sets of liquid-liquid interaction parameters, $a_{ow}=100,120$ and 150. Increasing a_{ow} results in a stronger repulsion and correspondingly higher interfacial tension between the two liquids. The snapshots for degradation of a nanogel particle at the interface with $a_{ow}=100,120$ and 150 are shown in Fig. 6a-c, Fig. 6d-f and Fig. 6g-i, respectively.

For the cases with higher repulsion ($a_{ow}=120$ and 150), all the fragments formed during degradation remain at the interface for the entire duration of the process (see Fig. 6d-i). A small fraction of fragments, such as fragments formed somewhat away from the interface (as the ones circled in Fig. 6e), diffuse within the liquid phase before adsorbing onto the interface. Once adsorbed at the interface, these fragments do not detach from the interface and remain adsorbed. For the case with $a_{ow}=100$ (the case with lowest interfacial tension considered), a notable fraction of fragments remains in the liquid phase without adsorption onto the interface (see Fig. 6a-c). This difference in adsorption is seen quantitatively in the evolution of the number of contacts between the beads of the two liquid phases in Fig. 7a.

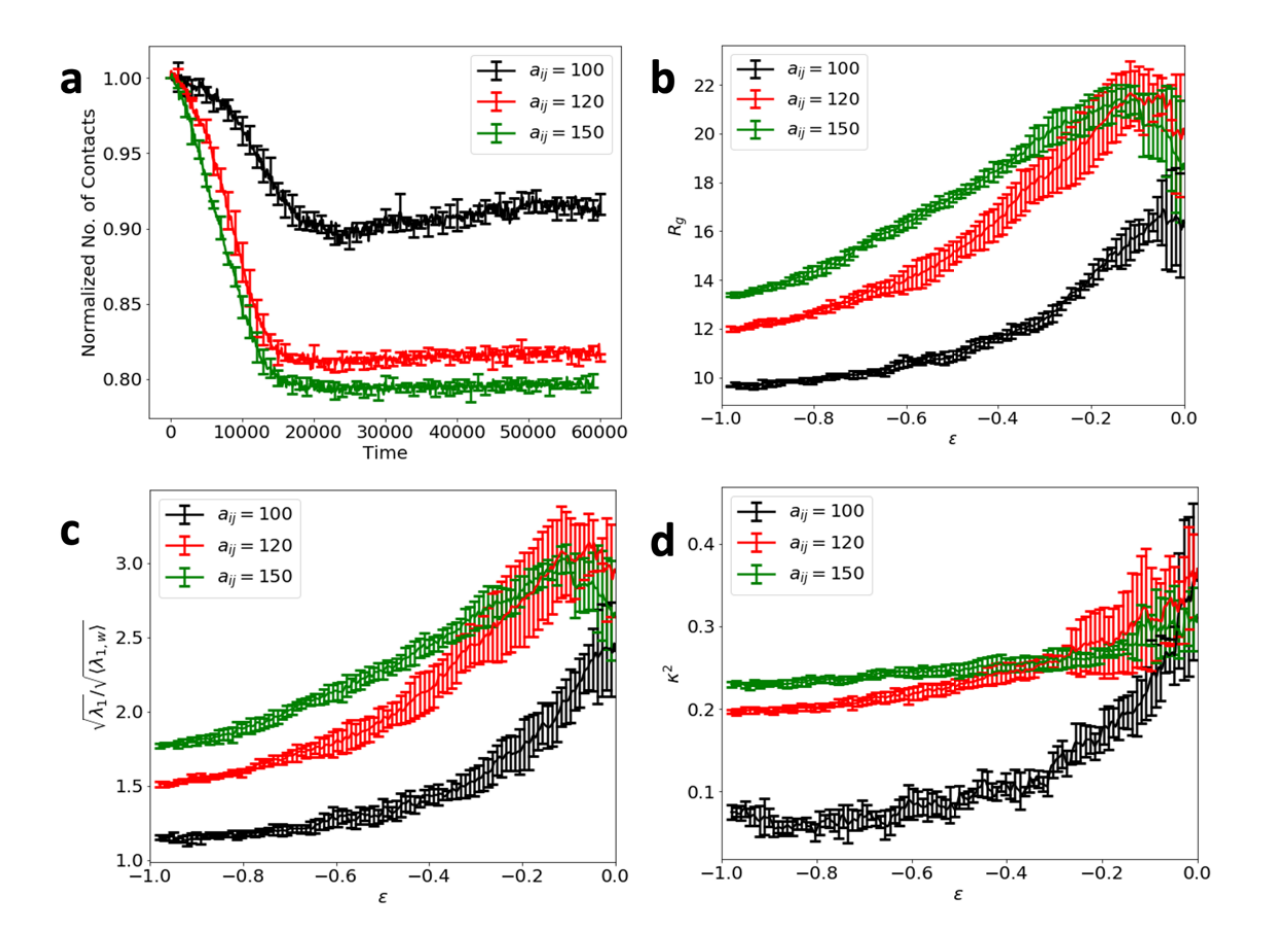


Figure 7. Effects of liquid-liquid interaction parameter. Evolution of (a) the number of contacts between two liquid phases, (b) radius of gyration, (c) extent of spreading, and (d) shape anisotropy for a nanogel particle degrading at the interface with $a_{ow} = 100$ (black curves), $a_{ow} = 120$ (red curves) and $a_{ow} = 150$ (green curves). All quantities are averaged over five simulations with error bars representing standard deviation. The data in (a) is normalized by the initial number of contacts for each case.

The cases of three different interfaces with $a_{ow}=100$, 120 and 150 are represented in Fig. 7 by black, red, and green curves, respectively. As the nanogel degrades at the interface, the number of contacts between the two liquids decreases due to spreading of the remnant nanogel and broken-off fragments over the interface. For the case of $a_{ow}=100$, this decrease is

relatively moderate with respect to the other two cases. The difference in the observed behavior can be attributed to the relatively smaller energy gain due to shielding of the unfavorable oil-water interactions upon fragment adsorption onto the interface. Our results show that this decrease in total interfacial energy due to spreading of small fragments at the interface with $a_{ow}=100$ is not sufficient to compensate for introducing relatively unfavorable contacts of polymer with oil with respect to that with water (recall that $a_{po}>a_{pw}$) along with the decrease in entropy due to interfacial confinement of these fragments. For the interfaces with $a_{ow}=120$ and $a_{ow}=150$, the decrease in interfacial energy upon fragment adsorption onto the interface is correspondingly higher, hence it is energetically favorable for the fragments to remain adsorbed decreasing the number of liquid-liquid contacts.

Evolution of the radius of gyration, extent of interfacial spreading, and shape anisotropy, κ^2 , of the nanogels with the proximity to the reverse gel point are provided in Fig. 7b-d. The extent of spreading, e, is defined as 19:

$$e(\epsilon) = \frac{\sqrt{\lambda_1(\epsilon)}}{\langle \sqrt{\lambda_1 w} \rangle},\tag{9}$$

where $\lambda_1(\epsilon)$ is the largest eigenvalue of the gyration tensor during degradation, and $\langle \sqrt{\lambda_{1,w}} \rangle =$ 5.58 is the average of the square root of the largest eigenvalue during equilibration in the water phase (Fig. S4a). All three characteristics provide information only about the remnant nanogel (the largest topological cluster in the system) and not about spreading of the smaller fragments. The initial values of R_g prior to degradation increase with an increase in a_{ow} . This trend is in

agreement with prior studies, which demonstrated enhanced stretching of nanogels at interfaces with higher interfacial tension¹⁷. Correspondingly, the initial extent of spreading for the nanogel at the interface with $a_{ow} = 100$ is the lowest ($e \approx 1.1$ prior to degradation) and increases with an increase in a_{ow} . In all cases considered, extent of spreading increases while approaching the reverse gel point, reaching nearly three-fold extension ($e \approx 2.75$) for the two interfaces with higher interfacial tension. Note that the relative extent of spreading with respect to that at the onset of degradation is most pronounced for the gels at the interface with $a_{ow} = 100$ (black curve in Fig. S4b). This difference in the relative extent of spreading can be understood by following variation in the shape anisotropy of the nanogels during their spreading over various interfaces. The gel adsorbed at the interface with relatively low interfacial tension ($a_{ow} = 100$) attains close to a hemispherical shape with $\kappa^2 \approx 0.10$ for the gel with chosen crosslink density. The same nanogel spreads and flattens more with an increase in a_{ow} , attaining more anisotropic shapes with values of $\kappa^2 \approx 0.20$ and $\kappa^2 \approx 0.22$ for the remaining two cases, respectively (thereby approaching 0.25 corresponding to a flat shape). As degradation occurs the κ^2 for nanogel at all interfaces increases with the increase being highest for the $a_{ow} = 100$ interface. Near the reverse gel point, nanogels at all three interfaces probed attain similar values of $\kappa^2 \approx 0.36$ with relatively large error bars. This value however remains lower than the values for the largest cluster at late times after the reverse gelation transition as reported above.

To summarize, these studies demonstrate that controlled degradation effectively promotes spreading of the remnant nanoparticle for all interfacial properties probed in this

work. Specifically, the extent of spreading increases with an increase in the extent of degradation. The nanogel attains relatively flat shapes during the entire degradation process for two cases of interfaces with relatively high interfacial tension. For the same two cases, the fragments broken-off from the nanogel are adsorbed onto the interface thereby notably decreasing a number of unfavorable oil-water contacts. For the lowest interfacial tension considered, large fraction of the broken-off fragments remains dispersed in the water phase. Hence, this study shows that controlled degradation can be used to promote spreading of the nanogels at the soft interfaces and concurrently control location of the broken-of fragments to either be dispersed in the good solvent or to be controllably deposited at the interface.

Conclusions

Via DPD simulations, we characterized the degradation of nanogels suspended in a solvent and those adsorbed at the liquid-liquid interface. In both scenarios, nanogels undergo a reverse gelation transition with the reverse gel point depending on the number of polymeric precursors constituting the original nanogel. We identified the reverse gel points in various scenarios via peak values of the reduced weight average degree of polymerization. Our results demonstrate that the reverse gel point follows a scaling relation $p_c^{\infty} + cN_p^{-\sigma}$ with respect to the number of polymer precursors , N_p , with the exponent $\sigma = 0.7$ and $p_c^{\infty} = 0.39$, which in turn is the value predicted by the bond percolation theory on a diamond lattice⁵⁷. Further, in both scenarios we characterized the structural characteristics of the remnant nanogels along

with the spatiotemporal distribution of polymeric fragments released during degradation as a function of proximity to the reverse gel point. Our results demonstrate district differences in structural characteristics of degrading nanogels depending on its environments. Nanogel degradation in a good solvent results in approximately uniform swelling of the remnant particle due to the decrease in crosslink density for the moderate relative extent of degradation reaction, $\epsilon \approx [-1:-0.38]$; within this range of ϵ , the particle keeps approximately spherical shape $(\kappa^2 \approx 0)$, while R_q gradually increases. On the contrary, the shape anisotropy κ^2 increases nearly monotonically from the onset of degradation with an increase in ϵ for the gels degrading at the interface, indicating that initial shape of the nanogel adsorbed at the interface is nearly immediately lost upon degradation since bond breaking promotes interfacial spreading. We demonstrate that the overall degradation process including mass loss from the nanogel is significantly affected by the nature of the polymer-solvent interactions. Further, for the nanogels initially adsorbed at the liquid-liquid interface, shape changes and spreading of the remnant nanogel along with dispersion of detaching fragments is affected significantly by the interfacial tension between the two incompatible liquids. For lower interfacial tension, some of the detaching fragments disperse to the liquid phase with higher affinity to polymer beads. Our results clearly demonstrate that controlled degradation of the nanogels adsorbed at liquid-liquid interfaces results in an enhanced extent of spreading and provides a means to control interfacial properties at the nanoscale. Further, our results provide insights on using

controlled degradation to dynamically tune shapes of nanocarriers and nanoscale topography at a liquid-liquid interface.

ASSOCIATED CONTENT

Supporting Information. Tables describing parameters corresponding to the degradation simulations in single solvent and at an interface and figures describing the following: nanogel as the largest connected cluster in the system, variation in reverse gel point across simulations, comparison of degradation and erosion in various solvents, shape of nanogel particle equilibrated in water. The following file is available free of charge:

SupportiongInformation.pdf

Data Availability Statement

The data underlying this study are openly available in the repository "Data for manuscript: Nanogel degradation at soft interfaces and in bulk: tracking shape changes and interfacial spreading" at https://doi.org/10.5281/zenodo.7410537.

AUTHOR INFORMATION

Corresponding author

Olga Kuksenok - Department of Materials Science and Engineering, Clemson University,

Clemson, South Carolina, 29634, United States;

orcid.org/0000-0002-1895-5206

E-mail okuksen@clemson.edu

Authors

Vaibhav Palkar - Department of Materials Science and Engineering, Clemson University,

Clemson, South Carolina, 29634, United States.

Devanshu Thakar - Department of Chemical Engineering, Indian Institute of Technology,

Gandhinagar, 382055, India

India

Notes

The authors declare no competing interests.

ACKNOWLEDGMENTS

The authors thank Dr. Pratyush Dayal and Eric Miller for valuable discussions. This work was

supported in part by the National Science Foundation under NSF Award No. 2110309. Any

opinions, findings and conclusions or recommendations expressed in this material are those of the

author(s) and do not necessarily reflect those of the National Science Foundation. Indian Institute

of Technology, Gandhinagar, is acknowledged for summer internship support of Devanshu Thakar

40

contribution. Clemson University is acknowledged for generous allotment of compute time on Palmetto cluster.

REFERENCES

- 1. Clegg, J. R.; Irani, A. S.; Ander, E. W.; Ludolph, C. M.; Venkataraman, A. K.; Zhong, J. X.; Peppas, N. A., Synthetic networks with tunable responsiveness, biodegradation, and molecular recognition for precision medicine applications. *Science Advances* **2019**, *5* (9).
- 2. Azagarsamy, M. A.; Alge, D. L.; Radhakrishnan, S. J.; Tibbitt, M. W.; Anseth, K. S., Photocontrolled Nanoparticles for On-Demand Release of Proteins. *Biomacromolecules* **2012**, *13*(8), 2219-2224.
- 3. Lu, Y.; Mei, Y.; Drechsler, M.; Ballauff, M., Thermosensitive core-shell particles as carriers for Ag nanoparticles: Modulating the catalytic activity by a phase transition in networks. *Angewandte Chemie-International Edition* **2006**, *45* (5), 813-816.
- 4. Kleinschmidt, D.; Nothdurft, K.; Anakhov, M. V.; Meyer, A. A.; Mork, M.; Gumerov, R. A.; Potemkin, I. I.; Richtering, W.; Pich, A., Microgel organocatalysts: modulation of reaction rates at liquid–liquid interfaces. *Materials Advances* **2020**, *1* (8), 2983-2993.
- 5. Destribats, M.; Lapeyre, V.; Wolfs, M.; Sellier, E.; Leal-Calderon, F.; Ravaine, V.; Schmitt, V., Soft microgels as Pickering emulsion stabilisers: role of particle deformability. *Soft Matter* **2011**, *7*(17), 7689-7698.
- 6. Miksch, C. E.; Skillin, N. P.; Kirkpatrick, B. E.; Hach, G. K.; Rao, V. V.; White, T. J.; Anseth, K. S., 4D Printing of Extrudable and Degradable Poly (Ethylene Glycol) Microgel Scaffolds for Multidimensional Cell Culture. *Small* **2022**, *18* (36), 2200951.
- 7. Scotti, A.; Schulte, M. F.; Lopez, C. G.; Crassous, J. J.; Bochenek, S.; Richtering, W., How Softness Matters in Soft Nanogels and Nanogel Assemblies. *Chemical Reviews* **2022**, *122* (13), 11675-11700.
- 8. Karg, M.; Pich, A.; Hellweg, T.; Hoare, T.; Lyon, L. A.; Crassous, J. J.; Suzuki, D.; Gumerov, R. A.; Schneider, S.; Potemkin, I. I.; Richtering, W., Nanogels and Microgels: From Model Colloids to Applications, Recent Developments, and Future Trends. *Langmuir* **2019**, *35* (19), 6231-6255.
- 9. Caldwell, A. S.; Aguado, B. A.; Anseth, K. S., Designing microgels for cell culture and controlled assembly of tissue microenvironments. *Advanced functional materials* **2020**, *30* (37), 1907670.

- 10. Brugger, B.; Richtering, W., Emulsions stabilized by stimuli-sensitive poly(N-isopropylacrylamide)-co-methacrylic acid polymers: Microgels versus low molecular weight polymers. *Langmuir* **2008**, *24* (15), 7769-7777.
- 11. Mourran, A.; Wu, Y. D.; Gumerov, R. A.; Rudov, A. A.; Potemkin, II; Pich, A.; Moller, M., When Colloidal Particles Become Polymer Coils. *Langmuir* **2016**, *32* (3), 723-730.
- 12. Klinger, D.; Landfester, K., Photo-sensitive PMMA microgels: light-triggered swelling and degradation. *Soft Matter* **2011**, *7*(4), 1426-1440.
- 13. Lopez, C. G.; Richtering, W., Does Flory-Rehner theory quantitatively describe the swelling of thermoresponsive microgels? *Soft Matter* **2017**, *13* (44), 8271-8280.
- 14. Hang, C.; Zou, Y.; Zhong, Y.; Zhong, Z.; Meng, F., NIR and UV-responsive degradable hyaluronic acid nanogels for CD44-targeted and remotely triggered intracellular doxorubicin delivery. *Colloids and Surfaces B: Biointerfaces* **2017**, *158*, 547-555.
- 15. Rumyantsev, A. M.; Gumerov, R. A.; Potemkin, I. I., A polymer microgel at a liquid–liquid interface: theory vs. computer simulations. *Soft Matter* **2016**, *12* (32), 6799-6811.
- 16. Geisel, K.; Isa, L.; Richtering, W., Unraveling the 3D localization and deformation of responsive microgels at oil/water interfaces: a step forward in understanding soft emulsion stabilizers. *Langmuir* **2012**, *28* (45), 15770-15776.
- 17. Vialetto, J.; Nussbaum, N.; Bergfreund, J.; Fischer, P.; Isa, L., Influence of the interfacial tension on the microstructural and mechanical properties of microgels at fluid interfaces. *Journal of Colloid and Interface Science* **2022**, *608*, 2584-2592.
- 18. Fernandez-Rodriguez, M. A.; Martin-Molina, A.; Maldonado-Valderrama, J., Microgels at interfaces, from mickering emulsions to flat interfaces and back. *Adv Colloid Interfac* **2021**, *288*.
- 19. Choudhury, C. K.; Palkar, V.; Kuksenok, O., Computational design of nanostructured soft interfaces: focus on shape changes and spreading of cubic nanogels. *Langmuir* **2020**, *36* (25), 7109-7123.
- 20. Zhang, X.; Malhotra, S.; Molina, M.; Haag, R., Micro-and nanogels with labile crosslinks–from synthesis to biomedical applications. *Chem Soc Rev* **2015**, *44* (7), 1948-1973.
- 21. South, A. B.; Lyon, L. A., Direct Observation of Microgel Erosion via in-Liquid Atomic Force Microscopy. *Chemistry of Materials* **2010**, *22* (10), 3300-3306.
- 22. Agrawal, G.; Wang, J. B.; Bruster, B.; Zhu, X. M.; Moller, M.; Pich, A., Degradable microgels synthesized using reactive polyvinylalkoxysiloxanes as crosslinkers. *Soft Matter* **2013**, *9*(22), 5380-5390.
- 23. Hwang, D. K.; Oakey, J.; Toner, M.; Arthur, J. A.; Anseth, K. S.; Lee, S.; Zeiger, A.; Van Vliet, K. J.; Doyle, P. S., Stop-flow lithography for the production of shape-evolving degradable microgel particles. *Journal of the American Chemical Society* **2009**, *131* (12), 4499-4504.
- 24. Smith, M. H.; Herman, E. S.; Lyon, L. A., Network deconstruction reveals network structure in responsive microgels. *The Journal of Physical Chemistry B* **2011**, *115* (14), 3761-3764.

- 25. Hoogerbrugge, P. J.; Koelman, J., Simulating microscopic hydrodynamic phenomena with dissipative particle dynamics. *Europhysics Letters* **1992**, *19*(3), 155-160.
- 26. Groot, R. D.; Warren, P. B., Dissipative particle dynamics: Bridging the gap between atomistic and mesoscopic simulation. *J. Chem. Phys.* **1997**, *107* (11), 4423-4435.
- 27. Español, P.; Warren, P. B., Perspective: Dissipative particle dynamics. *The Journal of Chemical Physics* **2017**, *146*(15), 150901.
- 28. Santo, K. P.; Neimark, A. V., Dissipative particle dynamics simulations in colloid and interface science: A review. *Adv Colloid Interfac* **2021**, 102545.
- 29. Feng, Y. H.; Zhang, X. P.; Zhao, Z. Q.; Guo, X. D., Dissipative Particle Dynamics Aided Design of Drug Delivery Systems: A Review. *Molecular Pharmaceutics* **2020**, *17* (6), 1778-1799.
- 30. Wang, X.; Santo, K. P.; Neimark, A. V., Modeling Gas—Liquid Interfaces by Dissipative Particle Dynamics: Adsorption and Surface Tension of Cetyl Trimethyl Ammonium Bromide at the Air—Water Interface. *Langmuir* **2020**, *36* (48), 14686-14698.
- 31. Santo, K. P.; Neimark, A. V., Effects of metal-polymer complexation on structure and transport properties of metal-substituted polyelectrolyte membranes. *Journal of Colloid and Interface Science* **2021**, *602*, 654-668.
- 32. Dutt, M.; Kuksenok, O.; Nayhouse, M. J.; Little, S. R.; Balazs, A. C., Modeling the Self-Assembly of Lipids and Nanotubes in Solution: Forming Vesicles and Bicelles with Transmembrane Nanotube Channels. *ACS Nano* **2011**, *5* (6), 4769-4782.
- 33. Vishnyakov, A.; Lee, M. T.; Neimark, A. V., Prediction of the Critical Micelle Concentration of Nonionic Surfactants by Dissipative Particle Dynamics Simulations. *J Phys Chem Lett* **2013**, *4*(5), 797-802.
- 34. Mills, Z. G.; Mao, W. B.; Alexeev, A., Mesoscale modeling: solving complex flows in biology and biotechnology. *Trends Biotechnol* **2013**, *31* (7), 426-434.
- 35. Wei, L.; Caliskan, T. D.; Tu, S.; Choudhury, C. K.; Kuksenok, O.; Luzinov, I., Highly Oil-Repellent Thermoplastic Boundaries via Surface Delivery of CF3 Groups by Molecular Bottlebrush Additives. *ACS Applied Materials & Interfaces* **2020**, *12* (34), 38626-38637.
- 36. Xiong, Y.; Choudhury, C. K.; Palkar, V.; Wunderlich, R.; Bordia, R. K.; Kuksenok, O., Mesoscale Modeling of Phase Separation Controlled by Hydrosilylation in Polyhydromethylsiloxane (PHMS)-Containing Blends. *Nanomaterials* **2022**, *12* (18), 3117.
- 37. Choudhury, C. K.; Kuksenok, O., Native-Based Dissipative Particle Dynamics Approach for α -Helical Folding. *The Journal of Physical Chemistry B* **2020**, *124* (50), 11379-11386.
- 38. Gao, L.; Xu, D.; Wan, H.; Zhang, X.; Dai, X.; Yan, L.-T., Understanding Interfacial Nanoparticle Organization through Simulation and Theory: A Review. *Langmuir* **2022**, *38* (37), 11137-11148.
- 39. Vishnyakov, A.; Mao, R.; Kam, K.; Potanin, A.; Neimark, A. V., Interactions of Crosslinked Polyacrylic Acid Polyelectrolyte Gels with Nonionic and Ionic Surfactants. *The Journal of Physical Chemistry B* **2021**, *125* (50), 13817-13828.

- 40. Yong, X.; Simakova, A.; Averick, S.; Gutierrez, J.; Kuksenok, O.; Balazs, A. C.; Matyjaszewski, K., Stackable, Covalently Fused Gels: Repair and Composite Formation. *Macromolecules* **2015**, *48* (4), 1169-1178.
- 41. Zhang, M.; Larison, T.; Tu, S.; Kuksenok, O.; Stefik, M., Effect of Fluorophobic Character upon Switching Nanoparticles in Polymer Films from Aggregated to Dispersed States Using Immersion Annealing. *ACS Applied Polymer Materials* **2022**, *4* (10), 7042-7053.
- 42. Kravchenko, V. S.; Gumerov, R. A.; Papadakis, C. M.; Potemkin, I. I., Self-Assembly of Molecular Brushes with Responsive Alternating Copolymer Side Chains. *Macromolecules* **2022**, *55* (22), 10176-10187.
- 43. Gumerov, R. A.; Filippov, S. A.; Richtering, W.; Pich, A.; Potemkin, I. I., Amphiphilic microgels adsorbed at oil—water interfaces as mixers of two immiscible liquids. *Soft Matter* **2019**, *15* (19), 3978-3986.
- 44. Schmidt, M. M.; Bochenek, S.; Gavrilov, A. A.; Potemkin, I. I.; Richtering, W., Influence of charges on the behavior of polyelectrolyte microgels confined to oil–water interfaces. *Langmuir* **2020**, *36* (37), 11079-11093.
- 45. Nickel, A. C.; Kratzenberg, T.; Bochenek, S.; Schmidt, M. M.; Rudov, A. A.; Falkenstein, A.; Potemkin, I. I.; Crassous, J. J.; Richtering, W., Anisotropic Microgels Show Their Soft Side. *Langmuir* **2022**, *38* (17), 5063-5080.
- 46. Geisel, K.; Rudov, A. A.; Potemkin, I. I.; Richtering, W., Hollow and core–shell microgels at oil–water interfaces: Spreading of soft particles reduces the compressibility of the monolayer. *Langmuir* **2015**, *31* (48), 13145-13154.
- 47. Gumerov, R. A.; Rumyantsev, A. M.; Rudov, A. A.; Pich, A.; Richtering, W.; Möller, M.; Potemkin, I. I., Mixing of Two Immiscible Liquids within the Polymer Microgel Adsorbed at Their Interface. *ACS Macro Letters* **2016**, *5* (5), 612-616.
- 48. Sirk, T. W.; Slizoberg, Y. R.; Brennan, J. K.; Lisal, M.; Andzelm, J. W., An enhanced entangled polymer model for dissipative particle dynamics. *J. Chem. Phys.* **2012**, *136* (13), 11.
- 49. Palkar, V.; Kuksenok, O., Controlling Degradation and Erosion of Polymer Networks: Insights from Mesoscale Modeling. *J. Phys. Chem. B* **2022**, *126*(1), 336-346.
- 50. Palkar, V.; Choudhury, C. K.; Kuksenok, O., Development of Dissipative Particle Dynamics framework for modeling hydrogels with degradable bonds. *Mrs Advances* **2020,** *5* (17), 927-934.
- 51. Azagarsamy, M. A.; McKinnon, D. D.; Age, D. L.; Anseth, K. S., Coumarin-Based Photodegradable Hydrogel: Design, Synthesis, Gelation, and Degradation Kinetics. *ACS Macro Lett.* **2014**, *3*(6), 515-519.
- 52. Madl, C. M.; Katz, L. M.; Heilshorn, S. C., Tuning Bulk Hydrogel Degradation by Simultaneous Control of Proteolytic Cleavage Kinetics and Hydrogel Network Architecture. *ACS Macro Lett.* **2018**, *7*(11), 1302-1307.
- 53. Sakai, T.; Matsunaga, T.; Yamamoto, Y.; Ito, C.; Yoshida, R.; Suzuki, S.; Sasaki, N.; Shibayama, M.; Chung, U. I., Design and fabrication of a high-strength hydrogel with ideally homogeneous network structure from tetrahedron-like macromonomers. *Macromolecules* **2008**, *41* (14), 5379-5384.

- 54. Truong, V. X.; Li, F. Y.; Forsythe, J. S., Photolabile Hydrogels Responsive to Broad Spectrum Visible Light for Selective Cell Release. *ACS Appl. Mater. Interfaces* **2017**, *9* (38), 32441-32445.
- 55. Villiou, M.; Paez, J. I.; del Campo, A., Photodegradable Hydrogels for Cell Encapsulation and Tissue Adhesion. *ACS Appl. Mater. Interfaces* **2020**, *12* (34), 37862-37872.
- 56. Griffin, D. R.; Kasko, A. M., Photoselective Delivery of Model Therapeutics from Hydrogels. *ACS Macro Lett.* **2012**, *1* (11), 1330-1334.
- 57. Stauffer, D.; Aharony, A., *Introduction To Percolation Theory*. Taylor & Francis: 1994.
- 58. Li, X.; Tsutsui, Y.; Matsunaga, T.; Shibayama, M.; Chung, U.; Sakai, T., Precise Control and Prediction of Hydrogel Degradation Behavior. *Macromolecules* **2011**, *44*(9), 3567-3571.
- 59. Warren, P. E. a. P., Statistical Mechanics of Dissipative Particle Dynamics. *EPL* (*Europhysics Letters*) **1995**, *30* (4), 191.
- 60. Groot, R. D.; Rabone, K. L., Mesoscopic Simulation of Cell Membrane Damage, Morphology Change and Rupture by Nonionic Surfactants. *Biophys. J.* **2001**, *81* (2), 725-736.
- 61. Lee, M.-T.; Mao, R.; Vishnyakov, A.; Neimark, A. V., Parametrization of Chain Molecules in Dissipative Particle Dynamics. *The Journal of Physical Chemistry B* **2016**, *120* (22), 4980-4991.
- 62. Metters, A.; Hubbell, J., Network formation and degradation behavior of hydrogels formed by Michael-type addition reactions. *Biomacromolecules* **2005**, 6(1), 290-301.
- 63. Nair, N.; Park, M.; Handgraaf, J.-W.; Cassiola, F. M., Coarse-Grained Simulations of Polymer-Grafted Nanoparticles: Structural Stability and Interfacial Behavior. *J. Phys. Chem. B* **2016**, *120* (35), 9523-9539.
- 64. Nikunen, P.; Karttunen, M.; Vattulainen, I., How would you integrate the equations of motion in dissipative particle dynamics simulations? *Computer Physics Communications* **2003**, *153* (3), 407-423.
- 65. Plimpton, S., Fast Parallel Algorithms for Short-Range Molecular Dynamics. *J. Comput. Phys.* **1995,** *117*(1), 1-19.
- 66. Thompson, A. P.; Aktulga, H. M.; Berger, R.; Bolintineanu, D. S.; Brown, W. M.; Crozier, P. S.; Veld, P. J. I.; Kohlmeyer, A.; Moore, S. G.; Nguyen, T. D.; Shan, R.; Stevens, M. J.; Tranchida, J.; Trott, C.; Plimpton, S. J., LAMMPS-a flexible simulation tool for particle-based materials modeling at the atomic, meso, and continuum scales. *Computer Physics Communications* **2022**, *271*.
- 67. Humphrey, W.; Dalke, A.; Schulten, K., VMD: Visual molecular dynamics. *Journal of Molecular Graphics & Modelling* **1996**, *14*(1), 33-38.
- 68. Liu, H.; Li, M.; Lu, Z. Y.; Zhang, Z. G.; Sun, C. C., Influence of Surface-Initiated Polymerization Rate and Initiator Density on the Properties of Polymer Brushes. *Macromolecules* **2009**, *42*(7), 2863-2872.
- 69. Singh, A.; Kuksenok, O.; Johnson, J. A.; Balazs, A. C., Tailoring the structure of polymer networks with iniferter-mediated photo-growth. *Polym. Chem.* **2016**, *7* (17), 2955-2964.

- 70. Singh, A.; Kuksenok, O.; Johnson, J. A.; Balazs, A. C., Photo-regeneration of severed gel with iniferter-mediated photo-growth. *Soft Matter* **2017**, *13* (10), 1978-1987.
- 71. Yong, X.; Kuksenok, O.; Matyjaszewski, K.; Balazs, A. C., Harnessing Interfacially-Active Nanorods to Regenerate Severed Polymer Gels. *Nano Letters* **2013**, *13* (12), 6269-6274.
- 72. Yong, X.; Kuksenok, O.; Balazs, A. C., Modeling free radical polymerization using dissipative particle dynamics. *Polymer* **2015**, *72*, 217-225.
- 73. Akkermans, R. L. C.; Toxvaerd, S.; Briels, W. J., Molecular dynamics of polymer growth. *J. Chem. Phys.* **1998**, *109* (7), 2929-2940.
- 74. Milchev, A.; Wittmer, J. P.; Landau, D. P., Formation and equilibrium properties of living polymer brushes. *J. Chem. Phys.* **2000**, *112* (3), 1606-1615.
- 75. https://docs.lammps.org/pair srp.html#pair-style-srp-react-command (accessed 11/21/2022).
- 76. Jha, P. K.; Zwanikken, J. W.; Detcheverry, F. A.; De Pablo, J. J.; de la Cruz, M. O., Study of volume phase transitions in polymeric nanogels by theoretically informed coarsegrained simulations. *Soft Matter* **2011**, *7*(13), 5965-5975.
- 77. Theodorou, D. N.; Suter, U. W., Shape of Unperturbed Linear-Polymers Polypropylene. *Macromolecules* **1985**, *18* (6), 1206-1214.
- 78. Tu, S. D.; Choudhury, C. K.; Giltner, M.; Luzinov, I.; Kuksenok, O., Mesoscale Modeling of Agglomeration of Molecular Bottlebrushes: Focus on Conformations and Clustering Criteria. *Polymers* **2022**, *14* (12).
- 79. Lee, H.; Baker, J. R.; Larson, R. G., Molecular dynamics studies of the size, shape, and internal structure of 0% and 90% acetylated fifth-generation polyamidoamine dendrimers in water and methanol. *J. Phys. Chem. B* **2006**, *110*(9), 4014-4019.
- 80. Jagodzinski, O.; Eisenriegler, E.; Kremer, K., Universal shape properties of open and closed polymer chains: Renormalization group analysis and Monte Carlo experiments. *Journal de Physique I* **1992**, *2* (12), 2243-2279.
- 81. Narros, A.; Moreno, A. J.; Likos, C. N., Effects of Knots on Ring Polymers in Solvents of Varying Quality. *Macromolecules* **2013**, *46* (9), 3654-3668.
- 82. Steinhauser, M. O., A molecular dynamics study on universal properties of polymer chains in different solvent qualities. Part I. A review of linear chain properties. *The Journal of Chemical Physics* **2005**, *122*(9), 094901.
- 83. Shy, L. Y.; Leung, Y. K.; Eichinger, B. E., CRITICAL EXPONENTS FOR OFF-LATTICE GELATION OF POLYMER-CHAINS. *Macromolecules* **1985**, *18*(5), 983-986.
- 84. Gupta, A. M.; Hendrickson, R. C.; Macosko, C. W., MONTE-CARLO DESCRIPTION OF AF HOMOPOLYMERIZATION DIFFUSIONAL EFFECTS. *J. Chem. Phys.* **1991**, *95* (3), 2097-2108.
- 85. Polanowski, P.; Jeszka, J. K.; Li, W. W.; Matyjaszewski, K., Effect of dilution on branching and gelation in living copolymerization of monomer and divinyl cross-linker: Modeling using dynamic lattice liquid model (DLL) and Flory-Stockmayer (FS) model. *Polymer* **2011**, *52* (22), 5092-5101.

- 86. Lin, T. S.; Wang, R.; Johnson, J. A.; Olsen, B. D., Topological Structure of Networks Formed from Symmetric Four-Arm Precursors. *Macromolecules* **2018**, *51* (3), 1224-1231.
- 87. Rankin, S. E.; Kasehagen, L. J.; McCormick, A. V.; Macosko, C. W., Dynamic Monte Carlo simulation of gelation with extensive cyclization. *Macromolecules* **2000**, *33* (20), 7639-7648.
- 88. Wang, R.; Lin, T. S.; Johnson, J. A.; Olsen, B. D., Kinetic Monte Carlo Simulation for Quantification of the Gel Point of Polymer Networks. *ACS Macro Lett.* **2017**, *6* (12), 1414-1419.
- 89. Rubinstein, M.; Colby, R. H., *Polymer Physics*. OUP Oxford: 2003.
- 90. Šomvársky, J.; Dušek, K., Kinetic Monte-Carlo simulation of network formation. *Polymer Bulletin* **1994**, *33* (3), 369-376.
- 91. Flory, P. J., *Principles of Polymer Chemistry*. Cornell University Press: 1953.
- 92. Spouge, J. L., EQUILIBRIUM RING FORMATION IN POLYMER-SOLUTIONS. *Journal of Statistical Physics* **1986**, *43* (1-2), 143-196.
- 93. Tanaka, Y.; Stanford, J. L.; Stepto, R., Interpretation of Gel Points of an Epoxy-Amine System Including Ring Formation and Unequal Reactivity: Measurements of Gel Points and Analyses on Ring Structures. *Macromolecules* **2012**, *45* (17), 7197-7205.
- 94. Lang, M.; Muller, T., Analysis of the Gel Point of Polymer Model Networks by Computer Simulations. *Macromolecules* **2020**, *53* (2), 498-512.
- 95. Sakai, T.; Katashima, T.; Matsushita, T.; Chung, U. I., Sol-gel transition behavior near critical concentration and connectivity. *Polym. J.* **2016**, *48* (5), 629-634.
- 96. Nishi, K.; Fujii, K.; Chung, U.; Shibayama, M.; Sakai, T., Experimental Observation of Two Features Unexpected from the Classical Theories of Rubber Elasticity. *Phys. Rev. Lett.* **2017**, *119* (26).
- 97. Watt, J.; Borhani, R.; Katsaggelos, A. K., Machine Learning Refined: Foundations, Algorithms, and Applications. *Machine Learning Refined: Foundations, Algorithms, and Applications* **2016**, 1-286.